EEET ECOLOGICAL ENGINEERING & ENVIRONMENTAL TECHNOLOGY

Ecological Engineering & Environmental Technology, 2026, 27(4), 118–136
https://doi.org/10.12912/27197050/218643
ISSN 2719–7050, License CC-BY 4.0

Received: 2026.02.16
Accepted: 2026.03.16
Published: 2026.04.01

Flood hazard assessment of the lower part of the Shkumbin River in the context of hydrological uncertainty

Olsi Barko[1*], Idlir Lami[1]

[1] Department of Hydraulics and Hydrotechnics, Polytechnic University of Tirana, 4 Deshmoret e Kombit Blvd., 1000 Tirana, Albania
* Corresponding author's e-mail: barkoolsi@gmail.com

ABSTRACT

The study aimed to improve flood hazard assessment in the lower reaches of the Shkumbin River (Albania) using two-dimensional modelling that takes into account hydrologic uncertainty of the flow. The study compared the extent of the hazard map where the maximum flow includes hydrological uncertainty versus that without hydrological uncertainty. The research methodology included statistical analysis of long-term hydrological observations (1949–1991) from the Rrogozhina hydrometeorological station and two-dimensional hydraulic modelling of floods for the lower reaches of the Shkumbin River, followed by hazard assessment using Australian classification approaches. This uncertainty was taken into account by accepting the upper limit of the confidence interval with 95% certainty when estimating quantiles for different return periods. The results of the study showed that the extent of the hazard map was directly affected by hydrological uncertainty. The flood hazard index assessment showed an expansion of the map for H1, H2, and H5 by 149%, 67%, and 50%, respectively, for a 100-year return period, confirming the high sensitivity of the floodplain system to hydrological uncertainty. The analysis confirmed the high sensitivity of the lower part of the Shkumbin River to intensive flood processes, which was reflected in the expansion of the risk areas. The analysis also confirmed the importance of the condition of the embankments, since it was precisely the damaged areas where their height is not according to the design that became the reason for the expansion of the flood. The results obtained can be used by water management institutions, spatial planning authorities and civil protection services to develop hazard maps, optimise flood management systems and plan sustainable infrastructure in floodplain areas.

Keywords: hydrological uncertainty, hazard map, modelling, flooding, inundation.

INTRODUCTION

In conditions of increased flow variability and precipitation intensity, reliable assessment of flood risk becomes particularly relevant. The coastal part of the Shkumbin River is classified as a high-risk area due to the low slope of the riverbed, which contributes to the formation of large areas of flooding. Protective embankments have been built here to reduce the scale of flooding, but their technical condition and anthropogenic changes in the relief remain critical factors. The territory is undergoing a gradual transition from agricultural use to more intensive recreational and infrastructural development, which increases the requirements for the accuracy of assessing potential flood threats. The uncertainty of hydrological parameters in such conditions can lead to incorrect forecasting of flood boundaries and ineffective engineering protection, which will increase the likelihood of damage to buildings, material losses and additional risks to the population.

Accurate consideration of hydrological uncertainty is necessary for the reliable determination of extreme flows and the construction of flood hazard maps [Huseynov et al., 2024; Knapik, 2025; Mossa, 2007; Piermattei et al., 2018]. The interaction of climatic, hydrological and model variability significantly increased the error in Qmax estimates, which was confirmed by the results of

Meresa et al. [2021], recording significant deviations under conditions of combined uncertainty. Additionally, the study determined that ignoring individual components of uncertainty leads to a systematic underestimation of maximum flows, which emphasised the need for careful consideration of variability factors. The study by Hu et al. [2020] demonstrated that the accuracy of frequency analysis depends on the length of the hydrological series and the statistical procedure, and a comparison of methods revealed significant differences in the determination of extreme values. The study also confirmed that different approaches to parameterisation caused noticeable variability in the results, complicating the interpretation of flood characteristics. According to Zhang et al. [2020], the critical role of the correct choice of theoretical distribution was proven, since the correct selection of the model increased the accuracy of Qmax estimates. The same study found that the Gumbel distribution best matched the empirical characteristics in many basins, outperforming other statistical models. Estimation of the upper limit of the confidence interval by Monte Censured increased stability of results, as observed in the work of Authors [2025], where this approach was more effective than standard methods. In addition, the use of the Monte Carlo method increased the accuracy of formalising uncertainty, confirming the advantages of more adaptive statistical procedures.

Albania's hydrological conditions determine the high sensitivity of river basins to flooding due to a combination of climatic, morphological and spatial factors. The spatial structure of precipitation significantly influences runoff formation, as demonstrated by the results of Lako and Kerpaci [2024]. The study demonstrated that combining climatic data with the morphometric characteristics of river basins increases the accuracy of regional hydrological assessments. The study of morphodynamic processes showed intensive erosion and accumulation, as indicated by the results of Hoxha [2021], and such changes weakened the stability of coastal slopes. The scientist found that changes in channel forms increased the risk of local destruction of hydraulic structures, as they increased the unevenness of flows in the coastal zone. The use of satellite technologies to record precipitation improved runoff modelling in the absence of ground-based observations, as demonstrated by the findings of Doko et al. [2022]. This is particularly relevant for mountainous and inaccessible areas, where spatial gaps in measurements cause significant uncertainty in reproducing the intensity and duration of precipitation. Flood risk assessments, according to Zaımı and Jaupaj [2020], demonstrated the high vulnerability of low-lying areas. Such areas remained vulnerable even during moderate rainfall events, as small changes in hydrological parameters can significantly increase the area of potential flooding.

Flood hazard modelling systems in the Western Balkan countries require adaptation to local geomorphological conditions, which determine the characteristics of extreme runoff formation. The use of universal risk assessment methods led to significant discrepancies in the mapping of flood zones, as shown by the conclusions of Ndini [2017], and the insufficient accuracy of the source data led to noticeable errors in the forecasts. Failure to incorporate local morphometric parameters weakened the reliability of the flood models. Climate variability affected the frequency of intense flood episodes, as demonstrated by the results of Deda et al. [2025]. The study also established that the expected increase in short-term storm events required mandatory consideration of future climate scenarios when assessing flood risks.

Previous studies did not sufficiently address the combination of local morphometric conditions, the accuracy of hydrological parameters, and the variability of runoff scenarios, which limited the reliability of flood hazard assessments. The study aimed to improve the accuracy of flood risk assessment in the lower reaches of the Shkumbin River by applying advanced two-dimensional hydraulic modelling, considering various maximum flow scenarios. To achieve this goal, it was necessary to perform the following tasks: analyse hydrological parameters and develop maximum water flow scenarios; simulate flooding using current spatial and hydraulic characteristics; and determine the boundaries, depths, and spatial changes of flooded areas for each calculated scenario.

MATERIALS AND METHODS

The study was conducted in September 2025 and was analytical and model-based, without field or experimental measurements. The object of modelling was the lower course of the Shkumbin River (Albania), including the estuary floodplain and adjacent lowland areas characterized by

increased flood vulnerability. The spatial extent of the modelled river section was approximately 35 km, the model area covered ~120 km², and the boundaries of the computational domain were defined by the river banks, major embankments, and floodplain limits.

Archival data from the Rrogozhina hydrometeorological station (1949–1991), stored at the Albanian Institute of Geosciences, Energy, Water and Environment, which is the official administrator of the national hydrological archives, were used for statistical analysis and hydraulic modelling. Separately, characteristics of flood events in 1959, 1962, 1963, 1971 and 1974, taken from hydrological bulletins stored in the National Library, were used. These years were included in the analysis because they are among the most representative and well-documented episodes of flood discharge, for which complete hydrographs and additional supporting information are available.

The criteria for the selection of flood recurrence intervals (T) were based on the provisions of Directive of the European Parliament and Council No. 2007/60/EC "On the Assessment and Management of Flood Risks" [2007], which provides for the development of flood hazard maps for scenarios with low, medium and high probability of flooding. Since the Directive does not specify specific numerical values for these intervals, the summary of international engineering practices presented in the review by Maranzoni et al. [2023] was addressed, which provides the ranges of recurrence intervals used in various European countries and the United States. Given Albania's geographical proximity to Italy and similar geomorphological conditions, the study uses the recurrence periods accepted in Italian practice: T=50 years (high probability), T=100 years (medium probability), and T=200 years (low probability).

Flood modelling was based on the calculation of unsteady flow, in which the change in discharge (Q) over time determines the dynamics of flooding, and peak discharge is a key input parameter of the hydraulic model. For this purpose, a statistical assessment of maximum flows was conducted based on a long-term series of observations obtained at a hydrometeorological station (Figure 1).

The methodological workflow followed a clear step-by-step procedure (Figure 1): data → statistical fitting → quantile estimation → hydrograph construction → hydraulic simulation → hazard classification

Data collection – long-term discharge observations (1949–1991) from the Rogozhina hydrometeorological station and historical flood hydrographs from selected years were compiled.

Maximum series generation – the annual maximum series (AMS) approach was applied, selecting the maximum daily discharge for each hydrological year, producing one peak per year. The series contained 43 observations. The peak over threshold (POT) method was not applied.

Homogeneity and stationarity testing – homogeneity of the AMS was tested using Pettitt and Mann-Kendall trend tests. Stationarity was assessed using the Mann-Kendall test for trends and visual inspection of the time series. No significant trends or non-stationarities were detected.

Statistical fitting – the series of annual maxima was fitted to theoretical extreme value distributions using the DSS algorithm [El Adlouni and Bobée, 2011]. Classical selection criteria, such as the Akaike Information Criterion, were used to choose the optimal model. The Gumbel distribution was selected, with parameters μ=636.52 and β=245.03.

Quantile estimation – using the fitted distribution, peak discharge quantiles for the selected recurrence intervals (50, 100, 200 years) were calculated. The Monte Carlo method was used to compute 95% confidence intervals.

Hydrograph construction – design hydrographs corresponding to each recurrence interval were generated based on the estimated peak discharges, including adjustments to match observed event shapes from historical floods.

Hydraulic simulation – the hydrographs were used as input for two-dimensional hydraulic modelling in HEC-RAS 2D v6.3, simulating unsteady flow and capturing spatial patterns of water depth, flow velocity, and flood extent.

Hazard classification: The product of flow depth (D) and velocity (V) was used to compute the integral intensity index (I). Flood hazard levels (H1–H6) were assigned according to the Australian vulnerability threshold approach, combining depth and velocity to assess risk for people, vehicles, and buildings.

To determine the optimal statistical model of the series of maximum discharges, its compliance with theoretical distributions was assessed using the DSS algorithm which is developed from El Adlouni and Bobée [2011] to help to the

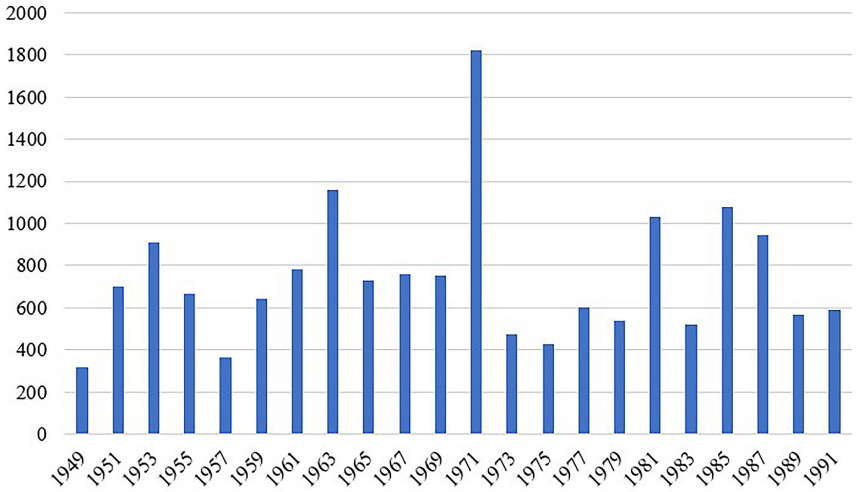

Figure 1. Maximum annual flow from 1949 to 1991

selection of the most appropriate class of distributions, with respect to extreme values. Once the class of the distributions is approved, the selection of an appropriate distribution from among the competitors within the class can be continued by means of classical tests and criteria, such as Akaike Information Criterion [Young et al., 1980]. The best fit was provided by the Gumbel distribution. The parameters of this model (μ=636.52, β=245.03) confirmed its adequacy for reproducing the variability of the series. and the 95% confidence intervals were estimated using a parametric Monte Carlo methode simulation with 10.000 iterations. At each iteration, the Gumbel distribution parameters (μ and β) were resampled according to their estimated uncertainty, allowing the propagation of parameter uncertainty to the quantiles. Both the uncertainty of the distribution parameters and the resulting quantiles were taken into account. (Figure 2).

For the accepted Gumbel distribution, peak flows were determined: approximately 1592 m^3/s for a 50-year recurrence period, 1763 m^3/s for 100 years, and 1934 m^3/s for 200 years, with corresponding 95% confidence intervals (Table 1).

While the peak flows, taking into account hydrological uncertainty, were accepted as the upper limit of the confidence interval with 95% certainty by MC method, resulting in: 1.843 m^3/s for a 50-year return period, 2.052 m^3/s for 100 years, and 2.261 m^3/s for 200 years, these values were used to construct design hydrographs for hydraulic modelling. The hydrographs were generated using a combination of historical event scaling and synthetic methods: observed historical hydrographs from well-documented floods (1959, 1962, 1963, 1971, 1974) were scaled proportionally to match the calculated peak discharges, preserving the observed flood shape, rise time, and recession characteristics. The hydrographs were asymmetrical, reflecting faster rising limbs and slower recession typical of the Shkumbin River flood events. Flood durations were defined based on the historical events, with total durations ranging from 12 to 36 hours, and rise times from 3 to 10 hours, depending on the recurrence interval. The soil conservation service (SCS) triangular method was not used, as historical scaling provided a more realistic representation of local flood dynamics.

The obtained maximum flow values were used as the main input parameters for two-dimensional hydraulic flood modelling. Hydraulic modelling was performed in an unsteady flow regime, in which changes in flow rate over time form the dynamics of the water level and the spatial distribution of flooding. This made it possible to reproduce the development of the flood process in real time and determine the maximum depths, flow velocities and flood area for the selected scenarios. The key input parameter of the model was the peak flow rate obtained from statistical analysis, as it determines the intensity of the flood wave and the potential scale of potentially dangerous hydraulic conditions. The modelling was performed in a two-dimensional environment using the HEC-RAS 2D v6.3 software package (Hydrologic Engineering Centre, U.S. Army Corps of Engineers, USA), which provides a spatial description of flow distribution and considers the interaction of water with relief features, including microtopographic features of the floodplain. During the numerical

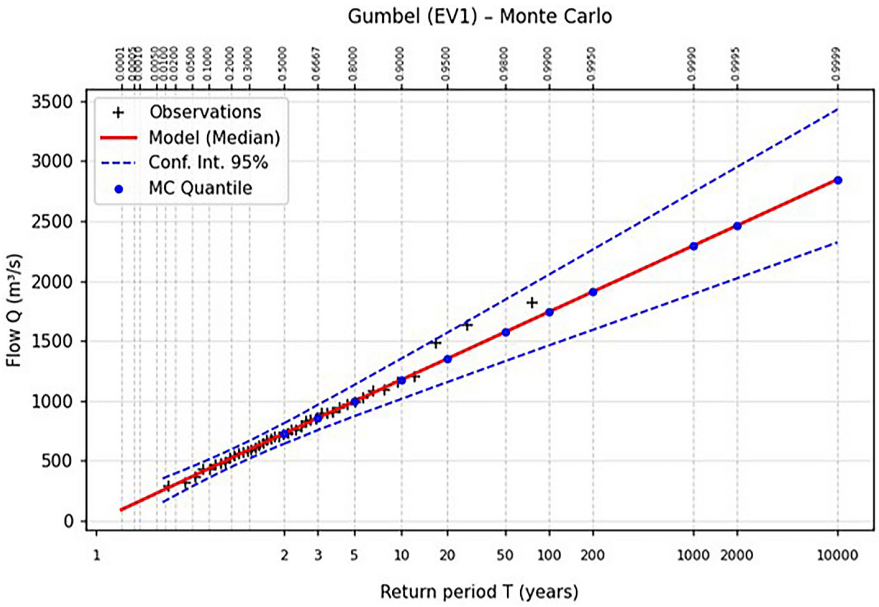

Figure 2. 95% confidence intervals by Monte Carlo method

Table 1. Quantiles and 95% CI

T	q	X_T (MLE)	Delta method	Monte Carlo method
			95% CI	95% CI
200	0.995	1934	1610–2300	1593–2261
100	0.99	1763	1480–2090	1463–2055
50	0.98	1592	1340–1870	1332–1845

calculation, the flow depth (D) and linear flow velocity (V) were determined; their product formed an integral intensity index (I), which was used to classify flood hazard levels and assess the potential impact on people, transport and buildings. Global satellite data were used for spatial model preparation: the Copernicus Global Dynamic Land Cover raster [Copernicus Global Land Service, 2025] to determine land use types and roughness parameters, as well as the digital elevation model of the State Authority for Geospatial Information of Albania, which provided the initial topographic framework for the model.

The Australian approach to flood risk assessment is based on the concept of vulnerability thresholds, which determine the ability of people, vehicles and buildings to withstand the effects of flooding. The methodology includes not only water depth or flow velocity separately, but also their combined effect, which reflects the overall intensity of the impact. This approach was used as it provides universal quantitative criteria for assessing hazards for different categories of objects and can be used to apply the results of hydraulic modelling in the form of standardised risk levels. Based on this indicator, six hazard levels (H1–H6) are formed, which were used to interpret the results of hydraulic modelling in the context of real threats. Class H1 describes conditions that are generally safe for people, vehicles and buildings. Level H2 corresponds to situations in which the flow becomes dangerous for small vehicles due to increased depth and speed. Class H3 reflects conditions that pose a threat to children, the elderly and drivers, as further increases in depth or speed reduce the stability of people and vehicles. Level H4 characterises the threat to people and vehicles due to increased traffic intensity. The highest hazard classes, H5 and H6, correspond to conditions in which all types of buildings are vulnerable to structural damage and people and vehicles cannot withstand the impact of the flow; class H6 covers cases where the integral intensity index exceeds the upper safety limit.

RESULTS

Seasonal characteristics of runoff formation in the Shkumbin River basin

Within the scope of the study, the nature of seasonal variability in runoff was analysed based on archival data for defferent years from 1962, 1963, 1971 and 1974 which are among the most representative and fully documented hydrological episodes in the studied basin. Based on these data, an intra-annual hydrograph was constructed, reflecting the dynamics of flow rates during the calendar year (Figure 3).

Analysis of the hydrograph showed that the maximum annual flow is generally distributed in the wet period of the year, which includes the period from October to February. The absolute maximum was about 1826 m^3/s, which indicates a combination of two key processes: intense precipitation and snowmelt in the mountainous areas of the upper reaches. Rapid and frequent increases in flow rates form a highly fragmented hydrograph, within which several short-term peaks are distinguished, which is characteristic of the Mediterranean rain-flood regime. The winter period is the main phase of runoff formation, where the bulk of the river volume is generated in a relatively short period of time [Grinfelde et al., 2021; Valujeva et al., 2018; Ongayev et al., 2024].

The dry period was characterised by the lowest flow values. During May-September, the flow remained mainly within the range of 25–60 m^3/s, while daily values rarely rose above 40 m^3/s. This stable minimum was caused by a prolonged lack of precipitation, high temperatures, and significant evaporation losses. The slight increases in flow to 70–90 m^3/s were local and short-lived, corresponding to episodic summer downpours, but they did not change the overall structure of low water levels. The summer regime was thus characterised by minimal variability and was a key phase against which the dynamics of flood periods were most clearly visible. In autumn, there was a gradual recovery in water levels. The overall dynamics of the hydrographs indicate a bimodal seasonal flow regime, where the main winter flood is combined with a secondary autumn rise, and the prolonged summer low water period forms the most stable phase of the annual cycle. This structure is typical for Mediterranean rivers with a pulsed water regime, which respond to short intense rains and demonstrate a low role of groundwater recharge. The identified patterns made it possible to justify the choice of a typical single hydrograph, which was formed based on representative flood events and used to construct hydrographs with different recurrence periods. This ensured the consistency of input data for further modelling of flood processes and facilitated the reproduction of the characteristic temporal structure of the flood wave for the Shkumbin River basin.

Flood isolation modelling

In order to reproduce the flood dynamics and assess the response of the river system to short-term intense disturbances, the most important flood episodes corresponding to the extreme event of 1962, 1963, 1971 and 1974 were selected (Figure 4). The selected cases are representative of the Shkumbin River basin, as it is characterized by sharp contrasts between low water levels and rapid formation of flood waves, which makes it possible to assess both the stability of the model to short-term strong peaks and its ability to reproduce gradual flow attenuation processes. In addition, these events have a high

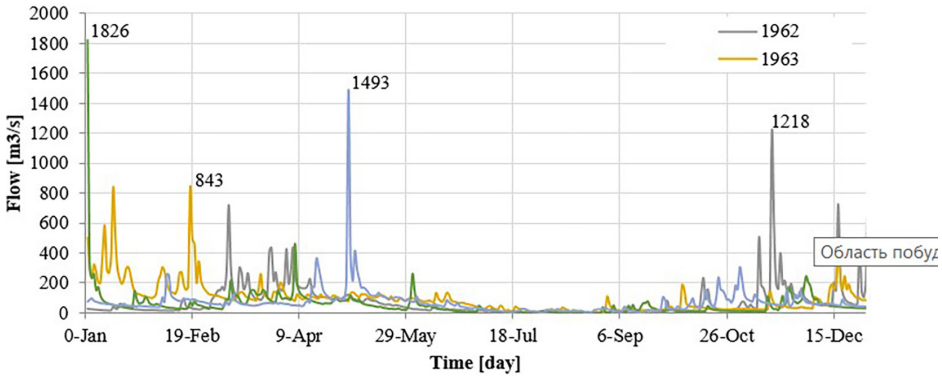

Figure 3. Intra-annual distribution of the Shkumbin River's flow

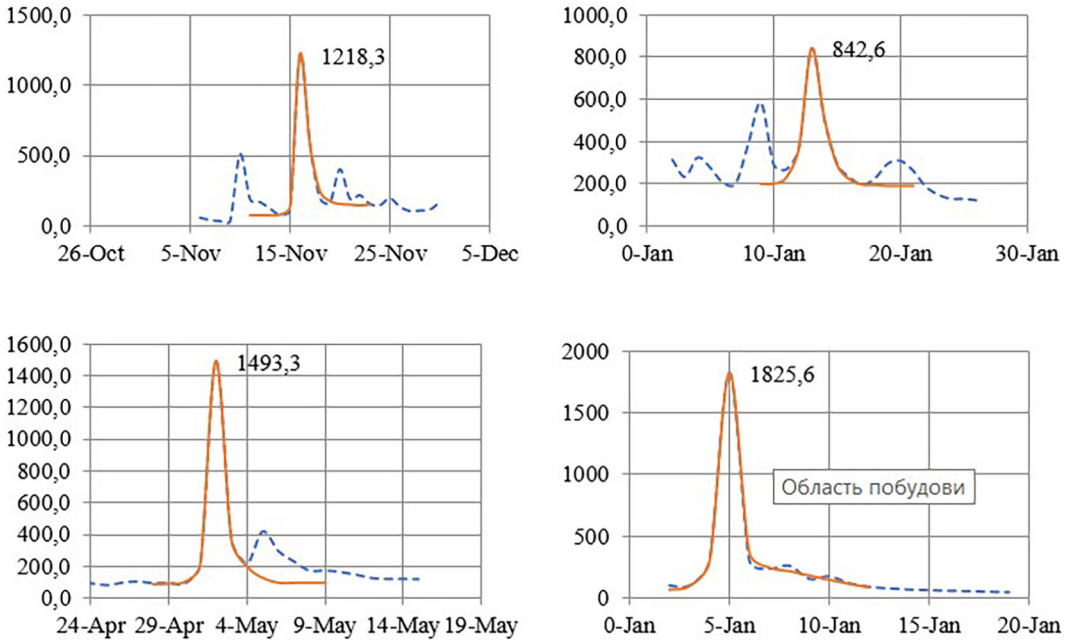

Figure 4. Hydrographs of the 1962, 63, 71, 74 flood event (isolated fragment of the flood wave)

level of documentation, which makes them a valuable empirical reference point for hydrodynamic modelling.

The hydrographs reflect the dynamics of the water flow in the lower reaches of the Shkumbin River from the beginning of the flood formation to its end, demonstrating the fluctuations in the flow characteristic of the winter rainy regime. The initial part of the curve is characterized by relatively low and stable flows in the range of 70–150 m^3/s, which corresponds to a period of limited surface runoff and the dominance of base flow. Against this stable background, there are isolated short-term increases, which are probably caused by episodic precipitation or short phases of partial snowmelt. These fluctuations were uneven and fragmentary in nature and did not lead to the formation of a full flood wave. Significant changes in the hydrodynamic picture occur during these periods, when the main flood wave is formed. This episode is highlighted in the graph with a red line, representing an isolated fragment of the flood, extracted from the general series for further hydraulic modelling. During this period, the flow rate increased sharply from approximately 100–200 m^3/s to maximum values over 1200–1800 m^3/s, i.e. more than tenfold. Such a rapid increase indicates intense precipitation in the context of increased soil moisture or the superposition of several hydrometeorological factors that led to the extremely rapid formation of surface runoff. The sharp shape of the flood peak also indicates the low buffer capacity of the floodplains in the phase of wave growth. In contrast to a sharp rise, the decline phase is longer and is characterized by a gradual decrease in flow over the next 7–8 days. This is a typical process for rain and snow floods, in which, after the end of the main cycle of precipitation, a significant delayed component remains, both in the form of depression runoff and due to groundwater drainage. The shape of the descending part of the red curve confirms the gradual release of accumulated water from flooded floodplains. The isolation of this red fragment from the full hydrograph is of methodological importance because it covers the critical interval of maximum hydrodynamic load. Thus, the red line represents not only an isolated flood wave, but also a key input scenario for the initial verification of the hydraulic model, which was used to assess its ability to accurately reproduce the mechanisms of local channel overload and interaction with floodplains. The floods of 1962, 1963, 1971, 1974 are representative events that can be used to assess the model's ability to adequately reproduce both rapid short-term changes in flow and prolonged processes of water level decline, which is key to building a comprehensive flood risk scenario.

Characteristics of representative flood events

Representative flood episodes from 1962, 1963, 1971, and 1974 were used to reproduce the temporal structure of the flood wave and construct

a unitary hydrograph, which subsequently served as the basis for hydraulic modelling. Preliminary processing included normalising the amplitude and duration of each event, which compared floods of different power and scale in a common dimensionless format. The results are presented in Figure 5, which shows individual hydrographs and their averaged representation.

Time series analysis shows that all flood events have a clearly asymmetrical shape: the rise front is characterised by a rapid increase in flow during the first 20–30% of the total duration, while the decline is much gentler and lasts 2–3 times longer than the rise period. This indicates the dominance of rapid runoff formation mechanisms (surface and slope runoff) in the rise phase and a significant contribution of floodplain accumulation processes in the decline phase. The most acute and concentrated rise was observed during the 1963 flood, which may indicate short-term but intense precipitation or increased soil saturation at the time of the event. In contrast, the floods of 1971 and 1974 show a prolonged decline, consistent with a possible delay in water retention in floodplain depressions and its slow return to the channel. The 1962 event has the shortest duration of the decline branch, reflecting a more "pulse-like" response mode of the basin. Despite differences in detail, the general nature of the curves indicates a high degree of structural similarity of flood waves in the basin, which provides grounds for the formation of a reliable averaged unitary hydrograph. Based on the averaged unitary hydrograph, complete hydrographs were formed for scenarios with recurrence periods of 50, 100 and 200 years. Their form is shown in Figure 6, which depicts the temporal evolution of flows for three characteristic scenarios.

A comparison of the indicators in Figure 3 shows that as the recurrence interval increases, the amplitude of the flood wave increases continuously: Q50 exceeds 1500 m^3/s, Q100 exceeds 1700 m^3/s and Q200 reaches 1900 m^3/s. In particular, the broadening of the peak part of the curve and the slower wave decay in high recurrence scenarios imply an increase in the duration of hazardous hydraulic conditions, especially in the upper parts of the floodplains and in areas with low slopes. This feature confirms the sensitivity of the Shkumbin basin to flood intensity: the higher the peak, the greater the increase in the period during which the flow velocity and depth remain critical.

To reflect hydrological uncertainty, additional hydrographs were generated based no MC method that include the upper limit of the 95% confidence interval, as shown in Figure 7. These curves demonstrate a systematic upward shift in peak values of 15–16%, depending on the iteration, which affects the further distribution of depths and velocities in the two-dimensional modelling.

A comparison of hydrographs for T=50, 100 and 200 years shows a regular increase in peak flows: approximately 1845 m^3/s for Q_{50}, approximately 2055 m^3/s for Q_{100} and 2261 m^3/s for Q_{200}. All curves retain a similar shape with an intense increase during the first 20-24 hours and an extended decline phase up to 96 hours, but the

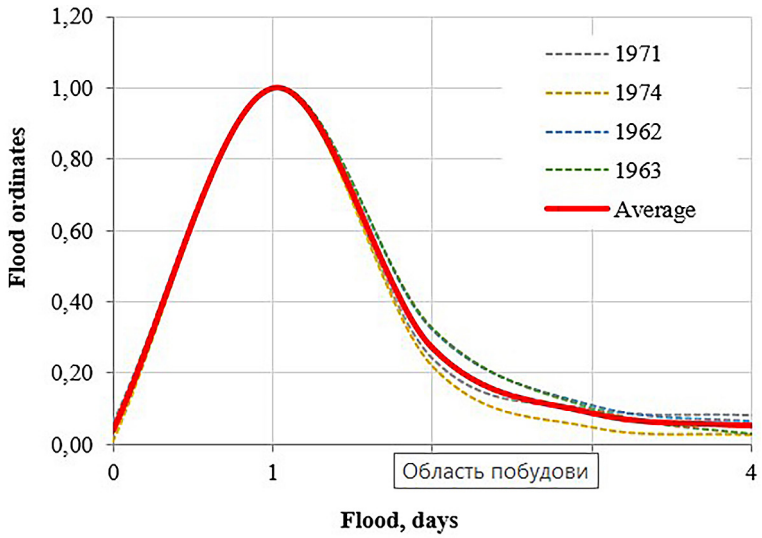

Figure 5. Standardised flood hydrographs for four representative years

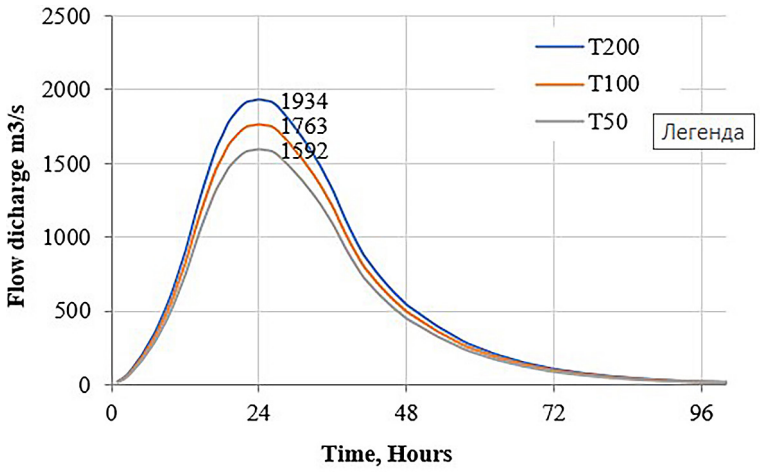

Figure 6. Hydrographs of runoff for T50-T200

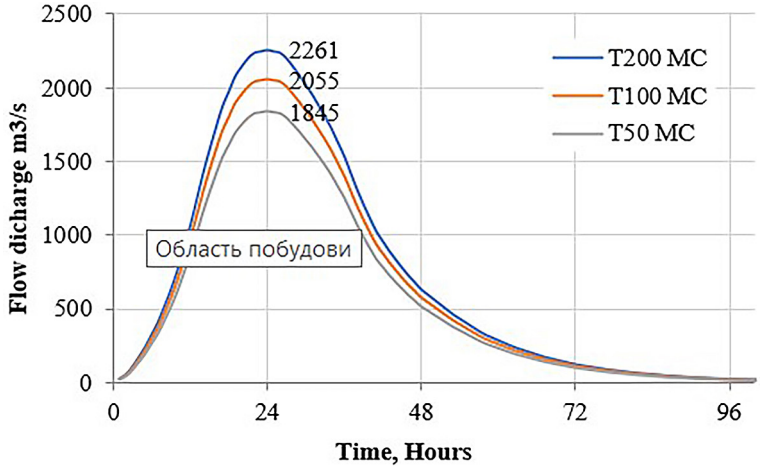

Figure 7. Hydrographs of runoff for T50MC-T200MC including hydrological uncertainty

increase in the recurrence period is accompanied by an expansion of the maximum flow plateau and an increase in the total water content of the wave. This means that a larger volume of water enters the river system in a short period of time. For the Q_{200} scenario, the duration of the decline phase of the wave increases significantly, indicating longer sustained high levels and increased stress on the channel, embankments and other hydraulic structures. A steeper front compared to Q_{50} indicates a faster rise in water levels, which increases the probability of local exceedance of the channel's capacity. Thus, with an increase in T, not only the peak intensity but also the duration of hazardous hydrodynamic conditions intensifies, which is critical for further assessment of flood risk.

Analysis of representative flood episodes confirmed their structural homogeneity and informativeness, which can be used for the construction of a universal unitary hydrograph suitable for correct scaling under various recurrence scenarios. The resulting hydrographs form a reliable basis for two-dimensional modelling and ensure a high level of reliability for further flood risk assessments.

Spatial modelling of flooding under various maximum runoff scenarios

Spatial modelling of flood processes in HEC-RAS 2D v6. 3 was used to recreate the morphodynamics of flooding for various probabilistic scenarios of maximum runoff (T=50, 100, and 200 years), providing an assessment of the depths, velocities, and area of water spread under the topographical conditions of the territory recorded in 2015. At this stage, it was necessary to utilise the digital elevation model and spatially differentiated land use characteristics that determine the hydraulic roughness of the surface.

The first step was to integrate land use maps based on Copernicus Global Dynamic Land Cover satellite data [Copernicus Global Land Service, 2025], which provide a high level of detail on the spatial structure of the surface. Figure 8 shows the main types of land cover that affect energy flow losses.

In particular, floodplain meadows and arable land are characterised by the lowest Manning's coefficient values (n=0.025–0.035), while forested areas and mixed forests have significantly higher roughness (n=0.12–0.14), which slows down the spread of the flood wave. These values are formally presented in Table 2, which is used by the model for spatial parameterisation of hydraulic resistance.

The second key element is digital elevation model, which ensured the reproduction of the elevation profile of the floodplain and riverbed with the necessary detail. Figure 9 demonstrates the terraces, side depressions and low-lying depressions that determine the trajectory and intensity of water flow.

These morphological relief structures are particularly relevant during peak flows, when overflowing of the main channel causes activation of side flows, formation of local wave fronts and redistribution of flow towards the lowest-lying areas of the floodplain. These topographic features, in particular the extensive depressions in the central and south-western parts of the model, determine the scale and configuration of potential flooding zones under the T=50–200 year scenarios.

To accurately reproduce the morphological features of the floodplain, a system of breaklines

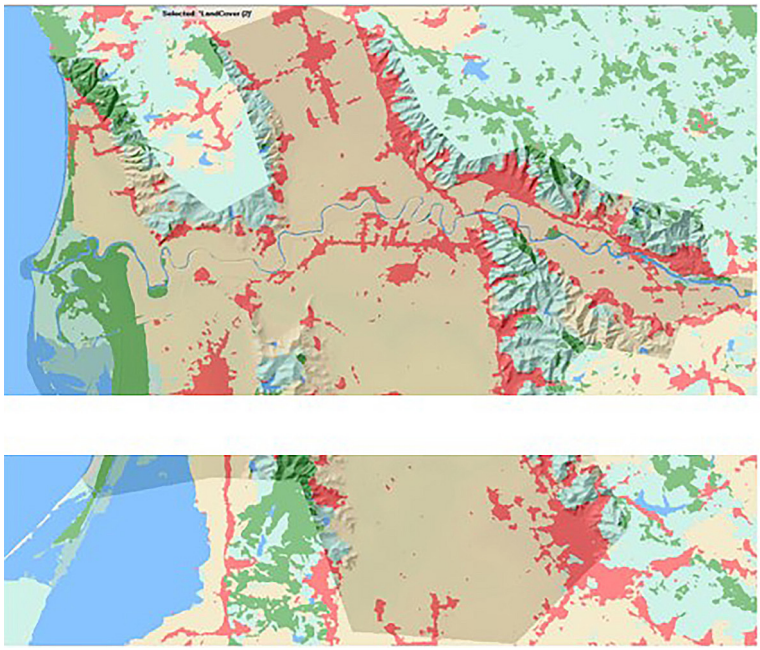

Figure 8. Spatial structure of land use in the modelling area according to Copernicus Global Dynamic Land Cover (2019)

Table 2. Classification of surface coating types and corresponding roughness parameters

ID	Surface type	Manning coefficient	Percentage of impermeability, %
0	NoData	0.035	0
1	Water	0.035	100
2	Trees	0.14	0
4	Flooded vegetation	0.04	0
5	Crops	0.03	0
6	Bare ground	0.025	0
7	Built Area	0.08	20
11	Mixed Forest	0.12	0

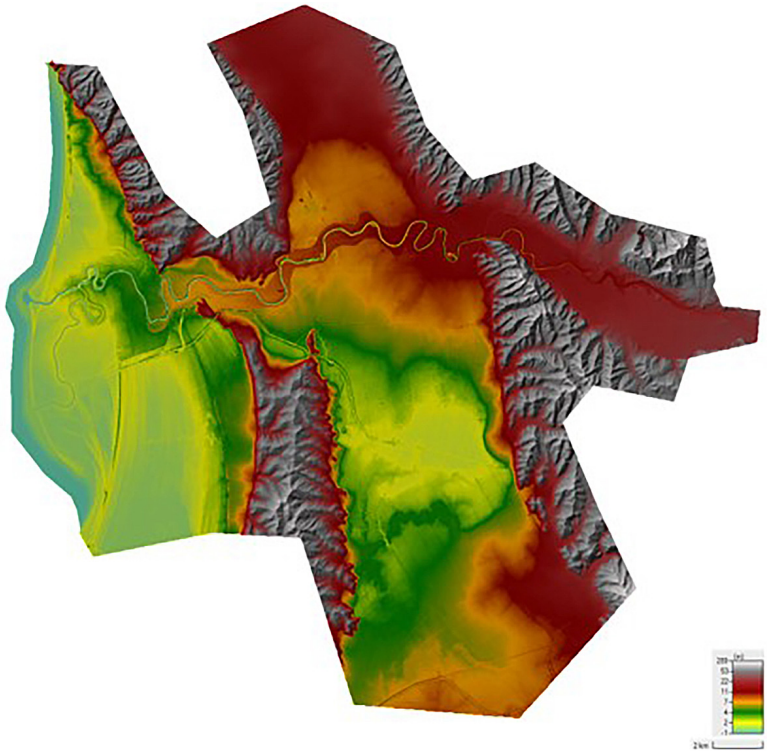

Figure 9. Digital elevation model with shadow relief for the lower reaches of the Shkumbin River

was introduced into the model, delineating channel edges, embankments, and other linear landforms (Figure 10a). Their integration into the grid ensures automatic densification of elements along these structures, which significantly improves the accuracy of modelling surface gradients and flow directions. The fragment of the calculation grid shows how breaklines control the shape and orientation of elements, preventing interpolation errors and incorrect reproduction of coastlines (Figure 10b).

The boundary conditions for modelling are shown in Figure 11, where the upper boundary corresponds to the point of input of maximum flow hydrographs (Q_{50}, Q_{100}, Q_{200} and Q_{50MC}, Q_{100MC}, Q_{200MC}), and the lower boundary corresponds to constant sea level conditions, which are typical for coastal areas with periodic tidal action. The choice of this particular scheme is justified by the stability of the numerical solution and the realism of the interaction between the flood flow and the lower reach.

After performing a dynamic calculation for each scenario, maps of maximum depths and maximum flood velocities were obtained, as well as spatially consistent flood hazard index maps. For analysis of the spatial distribution of flooding, the most informative are the index maps, which integrate data on depth, velocity, and potential danger to people and infrastructure.

Figure 12a shows that for a 50-year recurrence interval, the main flood risk areas are concentrated in the strip adjacent to the riverbed. The highest hazard classes (4–6) tend to be found in meandering riverbed sections and narrow floodplain corridors, where the hydraulic gradient and local velocities increase due to riverbed narrowing. When hydrological uncertainty is taken into account (Figure 12b), the spatial pattern of risk remains similar, but the distribution of hazard classes changes markedly. The share of the lowest hazard class (H1) more than doubles (+102.83%), while class H5 increases by 58.34% and classes H2 and H4 increase slightly (+2.51% and +11.26%, respectively). In contrast, class H3 shows a small reduction (-4.31%), indicating that many cells are reclassified either towards lower or higher hazard levels. These changes illustrate that even a moderate increase in peak flows can substantially modify the internal structure of the hazard field, shifting large areas from intermediate to extreme classes.

For the T=100 years scenario presented in Figure 13a, the flood extent increases significantly, covering large areas of the left and right bank lowlands. The highest hazard

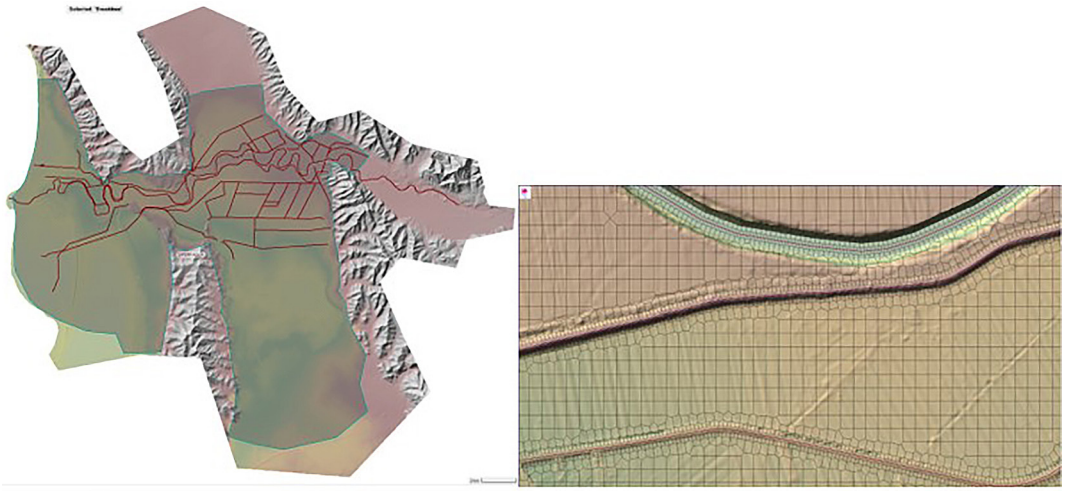

Figure 10. Breaklines and calculation grid structure of the HEC-RAS 2D v6.3 model: a) spatial arrangement of breaklines within the model; b) detailing of the calculation grid along th breaklines

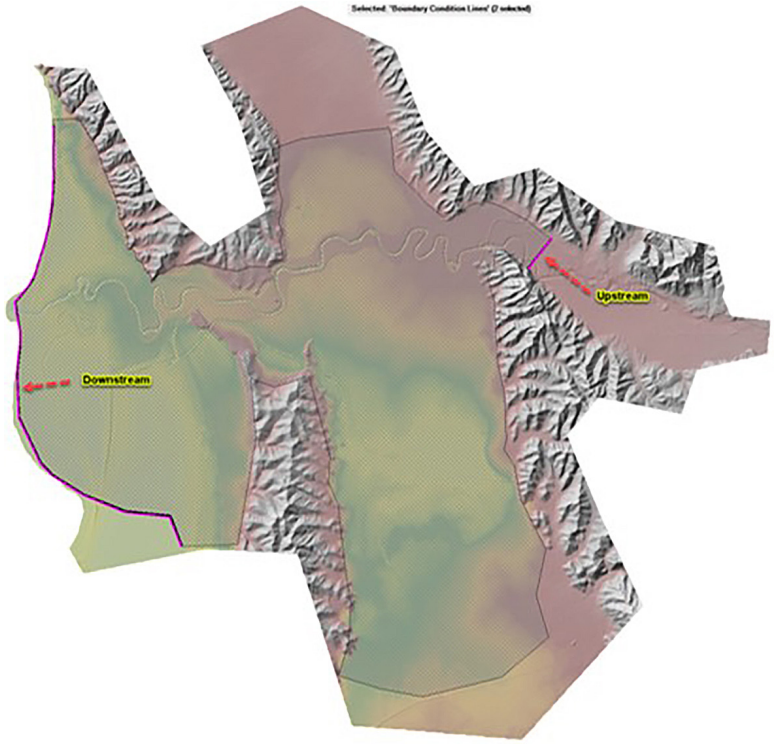

Figure 11. Boundary condition lines for the 2D model of the lower reaches of the Shkumbin River

classes are concentrated in areas of local depressions and dam breaches, indicating their insufficient resistance to flood-wave loads. In the variant including hydrological uncertainty (Figure 13b), there is an additional expansion of high-risk zones along floodplain channels and side drains, which is quantitatively reflected in Figure 16. The relative share of classes H1 and H2 increases sharply (+149.32% and +67.80%), while the intermediate classes H3 and H4 show only minor changes (+3.31% and +3.63%). At the same time, the very high hazard class H5 increases by 50.4% and class H6 by 9.02%. This pattern suggests that the uncertainty in peak discharge primarily leads to a strong growth of both low and very high hazard areas, with relatively stable proportions of the intermediate classes.

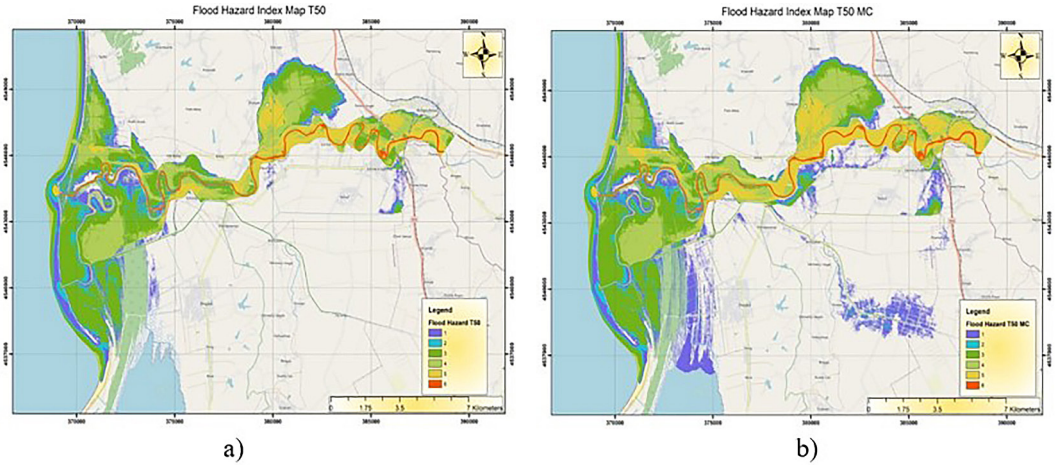

Figure 12. Flood hazard index maps for scenario T50: a) flood hazard index map for a return period of T50 (baseline modelling); b) flood hazard index map for a return period of T50, covering hydrological uncertainty

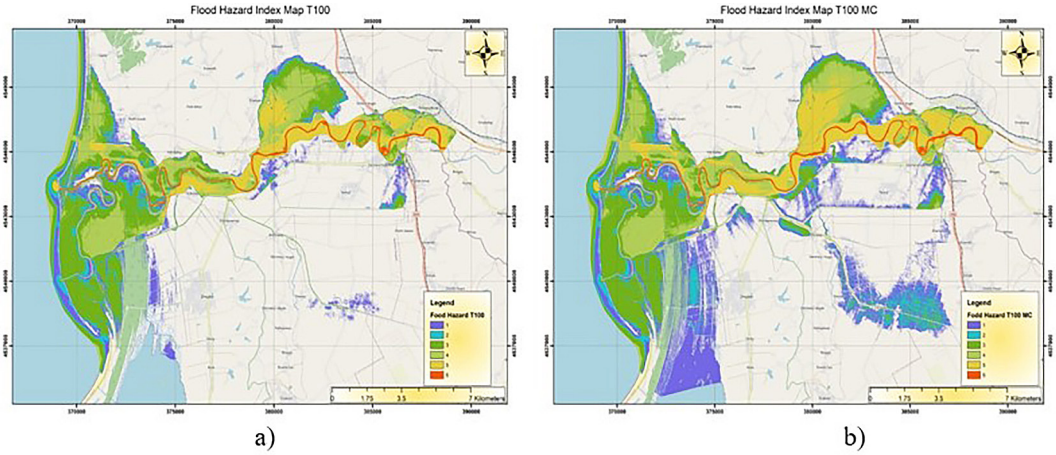

Figure 13. Flood hazard index maps for scenario T100: a) flood hazard index map for a return period of T100 (baseline modelling); b) flood hazard index map for a return period of T100, covering hydrological uncertainty

In the T=200 years scenario (Figure 14a), spatial modelling shows the maximum development of flood hazard: flooding covers almost the entire floodplain of the lower Shkumbin River, and class 5–6 zones are concentrated along meanders and in areas with locally lowered dams. The penetration of the flow into coastal settlements and agricultural land indicates that the capacity of the riverbed and floodplain has been exceeded. When hydrological uncertainty is incorporated (Figure 14b), the pattern of relative class changes (Figure 17) is very similar to that of the T100 scenario: the area of class H1 increases by about 149%, class H2 by approximately 68%, while classes H3 and H4 grow only slightly (about 3–4%). The very high hazard classes again show a pronounced rise, with class H5 increasing by 50.40% and class H6 by 9.02%. This confirms that under extreme events, even small additional increases in peak flow cause a disproportionate expansion of both low- and very high-hazard zones.

The flood hazard index maps for scenarios T50, T100 and T200 (Figures 12–14), together with the class-change analysis (Figures 15–17), provide a consistent basis for integrated hazard assessment. Index classes 4–6 delineate zones of high and very high hazard, where the probability of population exposure and structural damage is greatest. When hydrological uncertainty is taken into account, the relative share of classes H5-H6 increases by about 50–60% and 7–9%, respectively, highlighting the strong sensitivity of the hazard index to variations in peak discharge and the potential amplification of extreme-risk areas.

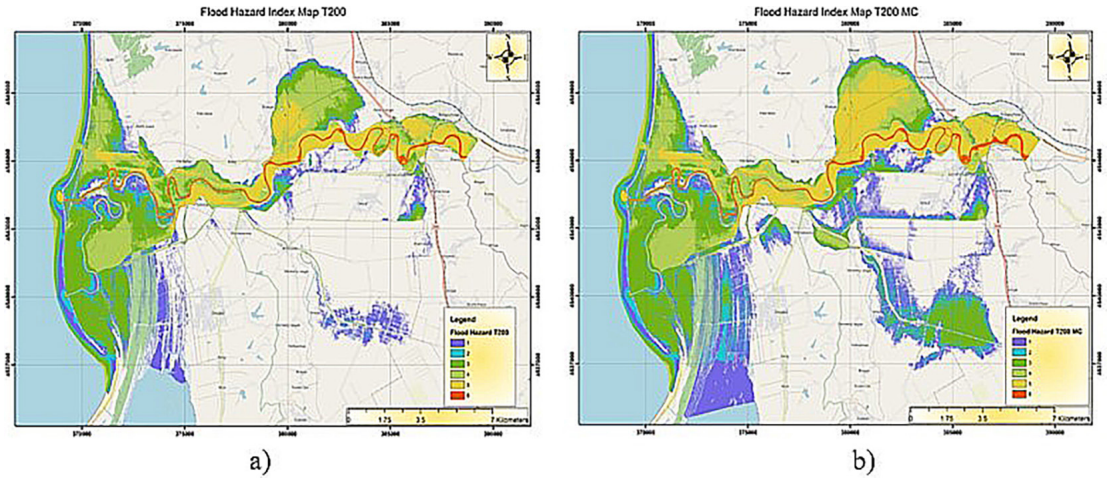

Figure 14. Flood hazard index maps for scenario T200: a) flood hazard index map for a return period of T200 (baseline modelling); b) flood hazard index map for a return period of T200, covering hydrological uncertainty

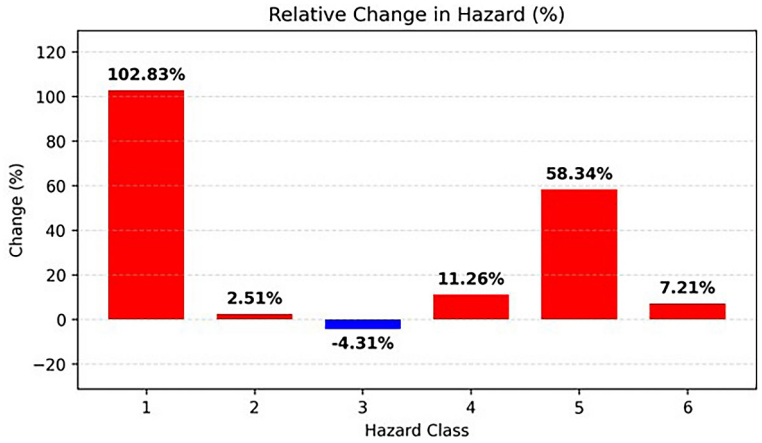

Figure 15. Comparison between flood hazard index maps for T50MC and T50

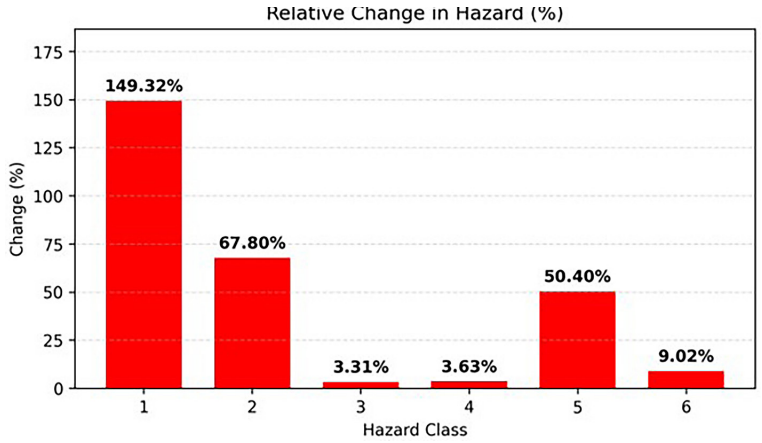

Figure 16. Comparison between flood hazard index maps for T100MC and T100

Overall, the results demonstrate a systematic increase in the scale and intensity of flooding with increasing recurrence period and confirm the critical role of embankment structures. In all scenarios, local underestimations of embankment crest levels determine the trajectory of the main breakthrough flows and the formation of secondary floodplain watercourses. The combined analysis of spatial patterns and hazard-class changes makes it possible to identify the areas of highest risk and to justify priority zones for engineering reinforcement of river coastal protection.

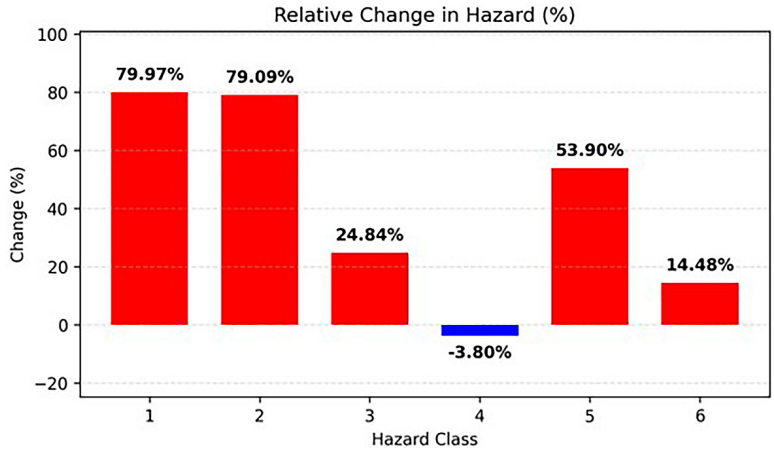

Figure 17. Comparison between flood hazard index maps for T200MC and T200

DISCUSSION

The results demonstrate the high sensitivity of the lower reaches of the Shkumbin River to variations in maximum flow and confirm the decisive role of the combined effects of hydrological uncertainty, floodplain morphometry and embankment crest conditions in the formation and spatial expansion of flood hazards. The integration of statistical analysis, unit hydrographs and two-dimensional modelling makes it possible to trace how increases in peak discharge and wave duration are translated into systematic growth and reclassification of flood-hazard index zones, causing a significant rise in threats to the population and infrastructure [Huseynli et al., 2024; Prajapati et al., 2025; Pinardi et al., 2016].

The intra-annual flow distribution (Figure 1) shows a markedly irregular regime, dominated by short-lived but very intense winter, spring and late-autumn peaks. In the representative years 1962, 1963, 1971 and 1974, individual floods reached about 843–1826 m^3/s, while for long periods outside these events the discharge remained comparatively low, typically within 25–60 m^3/s or below 100 m^3/s. This contrast between high, short-duration peaks and extended low-flow intervals confirms that the hydrological regime of the lower Shkumbin is controlled by impulse precipitation and rapid snowmelt events superimposed on a generally modest baseflow. A similar seasonal contrast was reported by Samantaray and Sahoo [2020], who showed that basins dominated by short-term convective storms exhibit abrupt, high peaks separated by extended recessions. The fragmentation of the hydrographs in Figure 1 is consistent with the pattern they described. Agreement is also found with the results of Faulkner et al. [2020], who demonstrated that non-stationary, extreme precipitation regimes intensify the severity and frequency of winter maxima. In contrast, Wijetunge and Neluwala [2023] analysed tropical catchments where storm surges drive much of the flood response; in the Mediterranean context of the Shkumbin, a mixed rain-snow mechanism remains dominant, but the high sensitivity of the system to short atmospheric impulses is comparable. A comparison with Curran et al. [2020] indicates that for many lowland rivers the duration of high stages is substantial, whereas in the Shkumbin, the most critical events tend to be more impulsive, a feature that strongly influences the subsequent hazard-index patterns.

Representative design hydrographs for return periods T50-T200 constructed from these conditions show an asymmetric wave shape, with a very steep rising limb that occupies only the first 20–30% of the event duration and a prolonged falling limb that lasts two to three times longer. Peak discharges for these scenarios reach approximately 1800–2300 m^3/s. Similar wave asymmetry was described by Williams et al. [2021], who identified substantial rising fronts followed by extended decline phases, closely resembling the behaviour of the Shkumbin floods. Their study, and that of Nones and Guo [2023], attributed the elongated recession to morphological buffering and temporary water storage on the floodplain – mechanisms that also explain the persistence of high hazard-index classes in depressions and inter-embankment corridors in the present modelling. In contrast, Zeiger and Hubbart [2021] documented more symmetric waves under uniform, long-lasting rainfall, indicating a weaker dependence of wave shape on relief than observed here, where topography plays a stronger controlling role. Ghimire et al. [2022]

further showed that two-dimensional hydraulic models are required to capture such asymmetry; one-dimensional schemes tend to smooth the rising limb and underestimate local extremes, which would misrepresent the areas of highest hazard index in the Shkumbin basin.

The peak-flow regime shown in Figure 1 is characterised by very rapid rises from baseflows of the order of 100–200 m^3/s to extreme values approaching 1800 m^3/s, followed by recessions that may last 7–8 days, reflecting slow drainage from floodplain storage. Parsons et al. [2020] showed that such rapid, high-amplitude peaks exert the greatest mechanical load on channels and embankments, which is consistent with the behaviour observed in the hydrographs of the lower Shkumbin. Muñoz et al. [2020] demonstrated that the combination of a very steep rising limb and a prolonged decline leads to long-lasting exceedance of critical water levels and a substantial increase in hazard, in line with the persistence of elevated hazard index classes in the modelled floodplain. By contrast, Tabari [2021] reported smoother, lower-amplitude peaks in multi-day events, which differ from the sharp peakiness evident in Figure 1. Brodie [2020] found a nonlinear relationship between duration and peak discharge, showing that short, intense pulses contribute disproportionately to maximum flows – again confirming the importance of the rapid rising limb for the development of extreme floods and very high hazard-index classes in the Shkumbin.

Spatial hydraulic-hazard modelling scenarios shows that the flood hazard index systematically reaches high and very high levels (H4–H6) over large areas of the floodplain. In the depth map zones classified as H4 generally correspond to inundation depths of roughly 2–3 m on the active floodplain, whereas classes H5 and H6 are linked to the deepest parts of the inundation field (typically >3–6 m) and are located predominantly within the protected corridor between the river embankments. These extreme classes are combined with locally high velocities, especially in meanders and inter-embankment corridors. When the upper limit of the 95% confidence interval for peak flows is considered, the extent of high-risk zones increases by about 12–27%, confirming the strong sensitivity of the floodplain system to variations in extreme hydrological parameters. A similar dependence of risk extent on changes in flow characteristics was demonstrated by Almazroui and Şen [2020], who showed that modest shifts in hydrometeorological extremes can significantly modify the configuration of hazardous areas. Hashemi-Beni and Gebrehiwot [2021] emphasised that correct classification of land-cover types improves the reconstruction of flood boundaries and depths; their findings are consistent with the influence of roughness variations on the spatial pattern of the hazard index in the lower Shkumbin. Kolaković et al. [2021] highlighted the decisive role of high-resolution digital terrain models obtained from LiDAR imagery. The present study follows this approach, using a high-resolution DTM to capture small-scale flow structures and local hazard hotspots that would be poorly resolved in coarser global products. Muthusamy et al. [2021] similarly confirmed the strong dependence of hydrodynamic behaviour on the spatial resolution of the digital elevation model, which is consistent with the marked sensitivity of floodplain depressions and embankment corridors in the Shkumbin Basin.

Analysis of the flood hazard index (H1–H6) and the comparative maps in Figures 13–15 show that increases in peak flows and the explicit consideration of hydrological uncertainty lead to a 15–30% expansion of hazardous areas (H3–H6), reflecting the strong responsiveness of the floodplain system to changes in hydrodynamic parameters. At the same time, the relative shares of the very high hazard classes H5 and H6 rise by about 50–60% and 7–9%, respectively, indicating a clear reorganisation of the hazard structure towards more extreme classes. This trend demonstrates that even moderate increases in maximum discharge, of the magnitude observed in Figure 1 and within the confidence limits of frequency analysis, can substantially transform the spatial configuration of hazard zones and intensify risks in the lower Shkumbin. Similar behaviour was reported by Soliman et al. [2022], who showed that changes in model parameters lead to noticeable reconfiguration of flood zones; their work also emphasised the role of land-use changes, which is consistent with the observed expansion of hazard-index areas. Alrammahi [2024] documented significant differences in risk patterns resulting from variations in hydraulic roughness, supporting the conclusion that surface characteristics strongly influence the distribution of vulnerable zones. By contrast, Osmanaj et al. [2025] found that in some basins the structure of risk zones is governed primarily by the frequency and intensity of extreme atmospheric events rather than hydraulic parameters alone – a partial contrast with the Shkumbin, where both factors interact. Zhllima et al. [2024] finally

confirmed the high infrastructure vulnerability of the region to increased hydrological loads, consistent with the observed expansion of flood-hazard index classes in this study.

In summary, the analysis shows that the flood dynamics of the lower Shkumbin River – as illustrated by the intra-annual distribution in Figure 1, the design hydrographs, and the hazard index maps – are controlled by a combination of increases in peak flow, strong flood-wave asymmetry, floodplain morphology and embankment crest conditions. Together, these factors determine both the expansion and the internal restructuring of hazard-index zones. The results are consistent with international studies that emphasise the leading role of hydrological variability, relief characteristics, surface parameters and the condition of river coastal protection structures in shaping extreme flood processes in diverse river systems.

CONCLUSIONS

Analysis of the seasonal structure of runoff based on the intra-annual hydrographs confirmed the dominance of short-lived but very intense winter, spring and late-autumn peaks, when discharges can rapidly rise to about 1800 m^3/s, while for long periods the flow remains below 100 m^3/s, with summer low flows typically within 25–60 m^3/s. This strongly contrasting regime shows that short-term atmospheric impulses control the rapidity of peak flows, whereas secondary autumn rises contribute to a partially bimodal distribution of water content. These patterns formed the basis for the selection of representative flood events and for the construction of a unit hydrograph with a steep rising limb and an extended recession, reproducing the limited storage capacity of the floodplain. Scaling this wave yielded peak values for the design scenarios T50–T200 (≈1592–1934 m^3/s), which represent a realistic spectrum of extreme events and provided a robust input for the subsequent hydraulic and hazard-index modelling.

Two-dimensional hydraulic simulations, carried out on a high-resolution digital terrain model, showed that with increasing return period the spatial extent and intensity of flooding systematically increase. Depths exceeding 1–1.5 m become widespread across the active floodplain, while in channel narrowings and inter-embankment passages local velocities exceed 2 m/s. The flood hazard index maps for T50, T100 and T200 demonstrated that high and very high hazard classes (H4–H6) are strongly controlled by floodplain morphology – depressions, meandering sections and directed-flow corridors – and that classes H5 and H6 are generally confined within the protected corridor between the river embankments. Incorporating hydrological uncertainty (upper limit of the 95% confidence interval for peak flows) led to a 15–30% expansion of hazardous areas (H3–H6) and to an increase in the relative shares of classes H5 and H6 by about 50–60% and 7–9%, respectively. This behaviour highlights both the strong sensitivity of the floodplain system to changes in peak discharge and the critical role of embankment-crest levels and local relief in shaping the configuration of high-risk zones.

The main limitation of the study is related to the hydrological input series, which is truncated and extends only until the early 1990s, leaving a gap with respect to recent decades and possible changes in flood regime. This temporal incompleteness may affect the representativeness of the derived design hydrographs and the ability to fully capture potential non-stationarity in extreme discharges. By contrast, the spatial data basis is robust: the digital terrain model has sufficiently high resolution and the adopted roughness coefficients are considered reliable for reproducing the main flow patterns, so that the spatial configuration of the hazard index can be regarded as well constrained. Future work should therefore focus primarily on extending and updating the discharge and rainfall records, testing non-stationary frequency models and alternative climate and land-use scenarios, and incorporating ensemble hydrological inputs. Such developments would improve the temporal representativeness of extreme-flow estimates and further strengthen the reliability of flood-hazard and hazard-index mapping for the lower Shkumbin River.

REFERENCES

1. Huseynov, Yu., Huseynli, J., Totubaeva, N., Guliyev, M., Mustafazada, Sh. (2024). Implementation of ESG criteria: Integration of environmental, social and governance criteria of companies in water management. *Scientific Horizons, 27*(7), 118–126. https://doi.org/10.48077/scihor7.2024.118
2. Knapik, M. (2025). Analysis of water leaks and savings strategies in commercial buildings and the impact of leed certification on water system operating cost. *Zeszyty Naukowe SGSP, 1*(95), 41–58. https://doi.org/10.5604/01.3001.0055.2863

3. Mossa, M. (2007). The floods in Bari: What history should have taught. *Journal of Hydraulic Research, 45*(5), 579–594. https://doi.org/10.1080/00221686.2007.9521795
4. Piermattei, V., Madonia, A., Bonamano, S., Martellucci, R., Bruzzone, G., Ferretti, R., Odetti, A., Azzaro, M., Zappalà, G., Marcelli, M. (2018). Cost-effective technologies to study the arctic ocean environment†. *Sensors (Switzerland), 18*(7), 2257. https://doi.org/10.3390/s18072257
5. Meresa, H., Murphy, C., Fealy, R., Golian, S. (2021). Uncertainties and their interaction in flood hazard assessment with climate change. *Hydrology and Earth System Sciences*, *25*(9), 5237–5257. https://doi.org/10.5194/hess-25-5237-2021
6. Hu, L., Nikolopoulos, E. I., Marra, F., Anagnostou, E. N. (2020). Sensitivity of flood frequency analysis to data record, statistical model, and parameter estimation methods: An evaluation over the contiguous United States. *Journal of Flood Risk Management*, *13*(1), e12580. https://doi.org/10.1111/jfr3.12580
7. Zhang, Z., Stadnyk, T. A., Burn, D. H. (2020). Identification of a preferred statistical distribution for at-site flood frequency analysis in Canada. Canadian Water Resources Journal, *45*(1), 43–58. https://doi.org/10.1080/07011784.2019.1691942
8. Authors. (2025). Estimation of the upper limit of confidence interval with the Monte Carlo method. Balkan *Journal of Interdisciplinary Research, 11*(1), 17–34. https://doi.org/10.2478/bjir-2025-0002
9. Lako, A., Kerpaci, A. (2024). Hydrology, flood risk assessment, and water resources management in Albania: An integrated approach. *Grassroots Journal of Natural Resources*, *7*(3), 1–21. https://doi.org/10.33002/nr2581.6853.070301
10. Hoxha, A. (2021). Influence of the morphodynamic factors on the territory of Albania. *KNOWLEDGE-International Journal, 49*(3), 571–576. https://ojs.ikm.mk/index.php/kij/article/view/4795
11. Doko, A., Maskey, S., Pérez, G.C. (2022). Integration of global rainfall data for hydrological forecasting in Albanian river catchments. *Albanian Journal of Natural and Technical Sciences, 56*(27), 45–59. https://akad.gov.al/wp-content/uploads/2024/07/03_Doko_Maskey_Albanian-Journal-of-Natural-and-Technical-Sciences_-20223-XXVII-56.pdf
12. Zaımı, K., Jaupaj, O. (2020). Flood forecasting in the western lowland of Albania with application of the hydrological modelling. *Journal of International Environmental Application and Science, 15*(4), 216–223. https://dergipark.org.tr/en/download/article-file/1464407
13. Ndini, M. (2017). Flood hazard and risk assessment. In E. Pojani & J. Keci (Eds.), *Risk Management in the Western Balkans* 46–58. Novi Sad: University of Novi Sad. http://kforce.gradjevinans.net/images/Fajlovi/Publications/EBook_Kforce_Disaster_risk_management_in_the_Western_Balkans_EN.pdf#page=56
14. Deda, M., Ndini, M., Lata, L. (2025). Climate variability and its impact on flood risk in the Vjosa river basin: An analysis of precipitation trends and vulnerability. In *Proceedings of the 20th Annual System of Systems Engineering Conference* 1–8. Tirana: IEEE. https://doi.org/10.1109/SoSE66311.2025.11083837
15. Directive of the European Parliament and Council No. 2007/60/EC "On the Assessment and Management of Flood Risks". 2007. http://data.europa.eu/eli/dir/2007/60/oj
16. Maranzoni, A., D'Oria, M., Rizzo, C. (2023). Quantitative flood hazard assessment methods: A review. *Journal of Flood Risk Management, 16*(1), e12855. https://doi.org/10.1111/jfr3.12855
17. El Adlouni, S., Bobée, B. (2011). Decision Support System for hydrological risk assessment. https://www.researchgate.net/publication/289215213_Decision_Support_System_for_hydrological_risk_assessment
18. Young, P., Jakeman, A., McMutrie, R. (1980). An instrumental variable method for model order identification. *Automatica, 16*(3), 281–294. https://doi.org/10.1016/0005-1098(80)90037-0
19. Grinfelde, I., Pilecka-Ulcugaceva, J., Bertins, M., Viksna, A., Rudovica, V., Liepa, S., Burlakovs, J. (2021). Dataset of trace elements concentrations in snow samples collected in Jelgava City (Latvia) in December 2020. *Data in Brief, 38*, 107300. https://doi.org/10.1016/j.dib.2021.107300
20. Valujeva, K., Burlakovs, J., Grinfelde, I., Pilecka, J., Jani, Y., Hogland, W. (2018). Phytoremediation as tool for prevention of contaminant flow to hydrological systems. *Research for Rural Development, 1*, 188–194. https://doi.org/10.22616/rrd.24.2018.029
21. Ongayev, M., Montayev, S., Denizbayev, S., Sakhipova, S. (2024). Hydrochemical characteristics of groundwater in Northwestern Kazakhstan aquifers: Implications for livestock water supply. *International Journal of Design and Nature and Ecodynamics, 19*(4), 1327–1340. https://doi.org/10.18280/ijdne.190425
22. Copernicus Global Land Service. (2025). Global Dynamic Land Cover. https://land.copernicus.eu/en/products/global-dynamic-land-cover
23. Huseynli, J., Huseynov, Yu., Kovalenko, O., Guliyev, M., Huseynova, L. (2024). Assessment of the impact of COP decisions on biodiversity and ecosystems. *Scientific Horizons, 27*(4), 128–140. https://doi.org/10.48077/scihor4.2024.128
24. Prajapati, M. B., Patel, R. B., Dogra, A. K., Singh, V., Kumar, P., Verma, S. (2025). Impact of water conservation on household end-use water consumption. In *Advancing Social Equity Through Accessible Green Innovation* 265–282. Pennsylvania: IGI Global. https://doi.org/10.4018/979-8-3693-9471-7.ch017

25. Pinardi, N., Lyubartsev, V., Cardellicchio, N., Caporale, C., Ciliberti, S., Coppini, G., De Pascalis, F., Dialti, L., Federico, I., Filippone, M., Grandi, A., Guideri, M., Lecci, R., Lamberti, L., Lorenzetti, G., Lusiani, P., Macripo, C. D., Maicu, F., Mossa, M., Tartarini, D., Trotta, F., Umgiesser, G., Zaggia, L. (2016). Marine rapid environmental assessment in the gulf of Taranto: A multiscale approach. *Natural Hazards and Earth System Sciences, 16*(12), 2623–2639. https://doi.org/10.5194/nhess-16-2623-2016
26. Samantaray, S., Sahoo, A. (2020). Estimation of flood frequency using statistical method: Mahanadi River basin, India. *H2Open Journal*, *3*(1), 189–207. https://doi.org/10.2166/h2oj.2020.004
27. Faulkner, D., Warren, S., Spencer, P., Sharkey, P. (2020). Can we still predict the future from the past? Implementing non-stationary flood frequency analysis in the UK. *Journal of Flood Risk Management*, *13*(1), e12582. https://doi.org/10.1111/jfr3.12582
28. Wijetunge, J.J., Neluwala, N.G. (2023). Compound flood hazard assessment and analysis due to tropical cyclone-induced storm surges, waves and precipitation: A case study for coastal lowlands of Kelani river basin in Sri Lanka. *Natural Hazards, 116*(3), 3979–4007. https://doi.org/10.1007/s11069-023-05846-w
29. Curran, A., De Bruijn, K.M., Kok, M. 2020. Influence of water level duration on dike breach triggering, focusing on system behaviour hazard analyses in lowland rivers. *Georisk: Assessment and Management of Risk for Engineered Systems and Geohazards*, *14*(1), 26–40. https://doi.org/10.1080/17499518.2018.1542498
30. Williams, B., Das, A., Luo, B., Lindenschmidt, K.E. (2021). An ice jam flood hazard assessment of a lowland river and its terminus inland delta. *Natural Hazards*, *105*(3), 2799–2817. https://doi.org/10.1007/s11069-020-04425-7
31. Nones, M., Guo, Y. (2023). Can sediments play a role in river flood risk mapping? Learning from selected European examples. *Geoenvironmental Disasters*, *10*(1), 20. https://doi.org/10.1186/s40677-023-00250-9
32. Zeiger, S.J., Hubbart, J.A. (2021). Measuring and modelling event-based environmental flows: An assessment of HEC-RAS 2D rain-on-grid simulations. *Journal of Environmental Management, 285*, 112125. https://doi.org/10.1016/j.jenvman.2021.112125
33. Ghimire, E., Sharma, S., Lamichhane, N. (2022). Evaluation of one-dimensional and two-dimensional HEC-RAS models to predict flood travel time and inundation area for flood warning system. *ISH Journal of Hydraulic Engineering, 28*(1), 110–126. https://doi.org/10.1080/09715010.2020.1824621
34. Parsons, M., Reeve, I., McGregor, J., Marshall, G., Stayner, R., McNeill, J., Hastings, P., Glavac, S., Morley, P. (2020). The Australian natural disaster resilience index volume I – State of disaster resilience report. https://hdl.handle.net/1959.11/29287
35. Muñoz, D.F., Moftakhari, H., Moradkhani, H. (2020). Compound effects of flood drivers and wetland elevation correction on coastal flood hazard assessment. *Water Resources Research, 56*(7), e2020WR027544. https://doi.org/10.1029/2020WR027544
36. Tabari, H. (2021). Extreme value analysis dilemma for climate change impact assessment on global flood and extreme precipitation. *Journal of Hydrology, 593*, 125932. https://doi.org/10.1016/j.jhydrol.2020.125932
37. Brodie, I. (2020). An evaluation of a multi-day rainfall-runoff volume-peak discharge transform for flood frequency estimation. *Australasian Journal of Water Resources, 24*(2), 167–182. https://doi.org/10.1080/13241583.2020.1821488
38. Almazroui, M., Şen, Z. (2020). Trend analyses methodologies in hydro-meteorological records. *Earth Systems and Environment, 4*(4), 713–738. https://doi.org/10.1007/s41748-020-00190-6
39. Hashemi-Beni, L., Gebrehiwot, A.A. (2021). Flood extent mapping: An integrated method using deep learning and region growing using UAV optical data. *IEEE Journal of Selected Topics in Applied Earth Observations and Remote Sensing, 14*, 2127–2135. https://doi.org/10.1109/JSTARS.2021.3051873
40. Kolaković, S., Fabian, J., Jeftenić, G., Trajković, S. (2021). River floodplain 1D/2D hydraulic modelling combined with recent LiDAR DTM technology. *Tehnički vjesnik, 28*(3), 880–890. https://doi.org/10.17559/TV-20200429024034
41. Muthusamy, M., Casado, M.R., Butler, D., Leinster, P. (2021). Understanding the effects of Digital Elevation Model resolution in urban fluvial flood modelling. *Journal of Hydrology, 596*, 126088. https://doi.org/10.1016/j.jhydrol.2021.126088
42. Soliman, M., Morsy, M.M., Radwan, H.G. (2022). Assessment of implementing land use/land cover LULC 2020-ESRI global maps in 2D flood modeling application. *Water, 14*(23), 3963. https://doi.org/10.3390/w14233963
43. Alrammahi, F.S. (2024). Identification of the changes in Manning's coefficient for Erbil Basin using the ArcGIS, HEC-RAS and remote sensing images. *AIP Conference Proceedings, 3249*, 070002. https://doi.org/10.1063/5.0236579
44. Osmanaj, L., Milevski, I., Aleksova, B. (2025). Integrated rainfall modelling and hydrometeorological alert system for extreme flooding in Kosovo. https://doi.org/10.21203/rs.3.rs-6917578/v1
45. Zhllima, E., Zdruli, P., Kullaj, E., Dobi, P. (2024). Adaptation to climate change in agriculture – status, gaps and recommendations in Albania. https://eu-4green.eu/wp-content/uploads/2025/02/Study-on-Climate-Change-Adaptation_Volume-II.pdf